

Galactic trajectories of interstellar objects 1I/'Oumuamua, 2I/Borisov, and 3I/ATLAS

Shokhruz Kakharov*^{ORCID} and Abraham Loeb*^{ORCID}

Astronomy Department, Harvard University, 60 Garden St., Cambridge, MA 02138, USA

Received 14 July 2025 / Accepted 11 February 2026

ABSTRACT

Aims. The first interstellar objects, 1I/'Oumuamua, 2I/Borisov, and 3I/ATLAS, were discovered over the past decade.

Methods. We follow the trajectories of known interstellar objects in the gravitational potential of the Milky Way galaxy to constrain their possible origin.

Results. We performed Monte Carlo orbital integrations using an ensemble of 10 000 trajectories per object to propagate measurement uncertainties in both object velocities and solar motion parameters through a Milky Way potential. We then used a Bayesian statistical framework that combines the resulting distributions of maximum vertical excursion (z_{\max}) with age–velocity–dispersion relations and star-formation-rate priors to infer plausible stellar ages.

Conclusions. Our Monte Carlo analysis yields median z_{\max} values of 0.016 ± 0.002 kpc for 1I/'Oumuamua, 0.121 ± 0.010 kpc for 2I/Borisov, and $0.481^{+0.023}_{-0.017}$ kpc for 3I/ATLAS. The Bayesian age inference indicates that 1I/'Oumuamua originated from a young stellar system (3.2 Gyr, 68% credible interval (CI): 0.5–8.8 Gyr), 2I/Borisov from an intermediate-age population (5.0 Gyr, 68% CI: 1.8–9.7 Gyr), and 3I/ATLAS from an old thick-disk source (8.7 Gyr, 68% CI: 5.2–10.3 Gyr). Taken together, these estimates are consistent with smaller vertical excursions tracing younger parent populations under our stated kinematic assumptions.

Key words. comets: general – minor planets, asteroids: general – comets: individual: 1I/'Oumuamua – comets: individual: 2I/Borisov – comets: individual: 3I/ATLAS

1. Introduction

The discovery of interstellar objects over the past decade has sparked significant interest in their origins and dynamics (see reviews by Siraj & Loeb (2022a), Jewitt & Seligman (2023), Jewitt (2024), and references therein). 1I/'Oumuamua was first reported in late 2017 (Meech et al. 2017; Williams 2017), and 2I/Borisov (C/2019 Q4) was identified in 2019 as an interstellar comet (Guzik et al. 2020). The more recent object, 3I/ATLAS (C/2025 N1), has been analyzed in subsequent kinematic studies (Seligman et al. 2025; Taylor & Seligman 2025). A fundamental question is the origin of each of these objects (Bailer-Jones et al. 2018; Bailer-Jones et al. 2020). Constraining their sources can shed light on the nature of these interstellar objects and the astrophysical processes that created them (see, e.g., Zhang & Lin 2020 and Loeb & MacLeod 2024).

In this paper, we numerically integrated the trajectories of interstellar objects backward in time in the gravitational potential of the Milky Way to relate them to potential stellar populations. We briefly review related work on kinematic age inference and backtracking (e.g., Almeida-Fernandes & Rocha-Pinto 2018; Hallatt & Wiegert 2020; Hsieh et al. 2021; Seligman et al. 2025); a complete comparison is presented in Sect. 4. Our Bayesian age-inference framework builds on prior kinematic approaches and complements association-based backtracking (e.g., Almeida-Fernandes & Rocha-Pinto 2018; Hsieh et al. 2021).

We implemented a Monte Carlo approach that addresses observational uncertainties through ensemble orbital calculations. Rather than computing single deterministic trajectories using published velocity measurements at face value, we generated 10 000 orbital realizations per object by sampling from the measurement uncertainty distributions. This methodology propagated both the formal errors in interstellar object velocities (derived from JPL Small-Body Database covariance matrices) and uncertainties in Solar motion parameters through the orbital calculations. Each Monte Carlo sample produced slightly different initial conditions, leading to a statistical distribution of maximum vertical heights (z_{\max}) that quantifies the uncertainty in our orbital predictions over gigayear timescales. We used the resulting distribution of maximum vertical excursions, z_{\max} , as a kinematic diagnostic of the likely ages of the parent stellar populations.

Since the scale height of stars in the Milky Way disk increases with age, we used the vertical excursion of each interstellar object from the Milky Way disk midplane to constrain its likely age. We developed a Bayesian statistical framework that combines the orbital z_{\max} measurements with models of stellar kinematics to infer the ages of the parent stellar systems. We evaluated the likelihood using the adopted vertical potential and an age–velocity–dispersion model (Sect. 3).

This paper is organized as follows. Sect. 2 describes our Monte Carlo orbital-integration methodology and the resulting ensemble statistics for the Galactic trajectories of individual interstellar objects, with subsections dedicated to 1I/'Oumuamua (Sect. 2.2), 2I/Borisov (Sect. 2.3), and 3I/ATLAS (Sect. 2.4). Sect. 3 presents our Bayesian statistical framework for age inference. Sect. 4 discusses prior work and places our results in

* Corresponding authors:
shokhruzbekkkakharov@college.harvard.edu;
aloeb@cfa.harvard.edu

context. Finally, Sect. 5 summarizes the implications of our results.

2. Galactic trajectories of interstellar objects

2.1. Method of calculation

Our numerical integration was based on the OrbitIntegrator from GalPot, which uses the MWPotential2014 model from McMillan (2017) to represent the gravitational potential of the Milky Way. We assumed a circular velocity of 233 km s^{-1} and an orbital radius of 8.3 kpc for the local standard of rest (LSR) around the Galactic center, consistent with the latest *Gaia* data (Pöder et al. 2023). We neglected transient non-axisymmetric features, which is a reasonable approximation for orbits in the outer disk. Over many orbital times, time-varying features can induce radial migration; by restricting our ensemble integrations to 1 Gyr, we focused on local dynamics, for which this approximation is adequate. Because both disk stars and interstellar objects (ISOs) are treated as collisionless tracers in the same potential, any such large-scale heating would similarly affect them. Therefore, our age inference depends on the present-day vertical excursion rather than the exact ejection epoch. We initialized the trajectories using each interstellar object’s velocity relative to the LSR and integrated them backward for 1 Gyr to obtain ensemble statistics. For visualization, we show longer integration windows, but all quantitative results reported in this section are based on the 1 Gyr integrations. We computed the orbits, extracted $R(t)$, $z(t)$, $\phi(t)$, and the velocity components $v_R(t)$, $v_z(t)$, and $v_\phi(t)$, and summarized the results using the maximum vertical excursion, z_{\max} .

To convert the velocity measurements in the Solar System to the Galactic frame of reference, we incorporated the motion of the Sun relative to the LSR, with Galactic velocity components $U_\odot = 10.79 \pm 0.56 \text{ km s}^{-1}$, $V_\odot = 11.06 \pm 0.94 \text{ km s}^{-1}$, and $W_\odot = 7.66 \pm 0.43 \text{ km s}^{-1}$ (Robin et al. 2022). Before entering the Solar System, 2I/Borisov’s velocity was $(U, V, W) = (33.1, -6.8, 8.3) \text{ km s}^{-1}$, while 1I/Oumuamua’s velocity relative to the Sun was $(U - U_\odot, V - V_\odot, W - W_\odot) = (-11.457 \pm 0.009, -22.395 \pm 0.009, -7.74 \pm 0.011) \text{ km s}^{-1}$ (Bailer-Jones et al. 2020; Mamajek 2017). For the interstellar object 3I/ATLAS (C/2025 N1), we adopted inbound heliocentric velocities of $(U, V, W) = (-54.4, -20.3, +19.5) \text{ km s}^{-1}$, derived from the JPL orbital solution JPL#5 (see also Seligman et al. 2025). The Galactocentric velocities were obtained via standard coordinate transformations that incorporate the solar-motion parameters.

Single-orbit calculations ignore observational uncertainties in both the interstellar object velocities and the solar-motion parameters. We therefore generated 10 000 orbital realizations per object by sampling

- measurement errors on the object velocities (from published covariance matrices);
- solar-motion uncertainties in (U, V, W) and in the rotation speed V_c .

For each realization, we transformed to the Galactic frame, integrated for 1 Gyr in the same potential, and recorded z_{\max} . We summarize each ensemble by its median and its 16th and 84th percentiles. The uncertainty budget is measurement-dominated; aside from the solar-motion and V_c uncertainties, we did not model additional systematic terms.

2.2. 1I/Oumuamua

Applying the Monte Carlo methodology described in Sect. 2.1, the ensemble analysis yielded a median maximum vertical excursion of $z_{\max} = 0.016 \text{ kpc}$. The corresponding trajectories

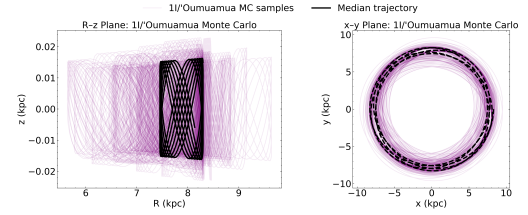


Fig. 1. Monte Carlo ensemble of 1I/Oumuamua trajectories in the $R - z$ plane. The transparent lines show 50 representative orbits from the uncertainty distribution, and the median trajectory is shown as a thick solid curve suitable for black-and-white printing.

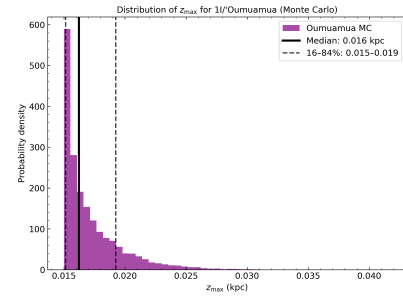


Fig. 2. Distribution of maximum vertical excursions z_{\max} for 1I/Oumuamua from our Monte Carlo analysis. The vertical lines indicate the median and the 16th and 84th percentiles.

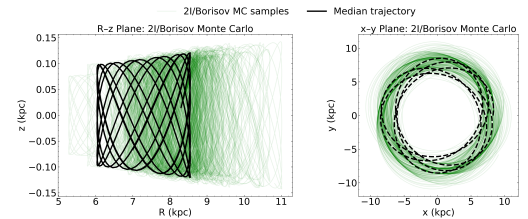


Fig. 3. Monte Carlo ensemble of 2I/Borisov trajectories in the $R - z$ plane. The transparent lines show 50 representative orbits from the uncertainty distribution, and the median trajectory is shown as a thick solid curve suitable for black-and-white printing.

in the $R - z$ plane are shown in Fig. 1, and the distribution of maximum vertical excursions z_{\max} is shown in Fig. 2. The 16th–84th percentile interval was 0.015–0.019 kpc, while the full Monte Carlo sample spanned 0.015–0.038 kpc. These small vertical excursions are suggestive of a young stellar origin; the corresponding age credible interval is reported in Sect. 3.

2.3. 2I/Borisov

The Monte Carlo trajectories of 2I/Borisov in the $R - z$ plane are shown in Fig. 3, and the resulting z_{\max} distribution is presented in Fig. 4. The ensemble analysis yielded a median maximum vertical excursion of $z_{\max} = 0.121 \text{ kpc}$. The 16th–84th percentile interval was 0.111–0.131 kpc, while the full Monte Carlo sample spanned 0.085–0.171 kpc. This intermediate z_{\max} value places 2I/Borisov in a regime consistent with moderately heated thin-disk stars, indicating that the comet’s vertical excursions are comparable to solar-type orbits.

2.4. 3I/ATLAS

Figure 5 displays the Monte Carlo $R - z$ trajectories for 3I/ATLAS, while Fig. 6 shows the corresponding distribution of maximum vertical excursions z_{\max} . The ensemble analysis yielded a median maximum vertical excursion of

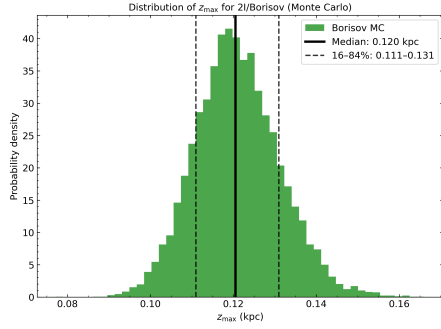


Fig. 4. Distribution of maximum vertical excursions z_{\max} for 2I/Borisov from our Monte Carlo analysis. The vertical lines indicate the median and the 16th and 84th percentiles.

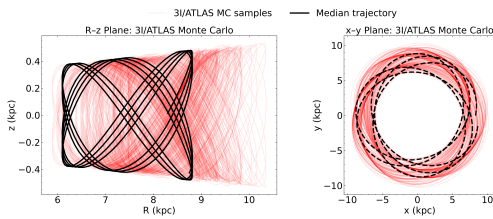


Fig. 5. Monte Carlo ensemble of 3I/ATLAS trajectories in the $R - z$ plane. The transparent lines show 50 representative orbits from the uncertainty distribution, and the median trajectory is shown as a thick solid curve suitable for black-and-white printing.

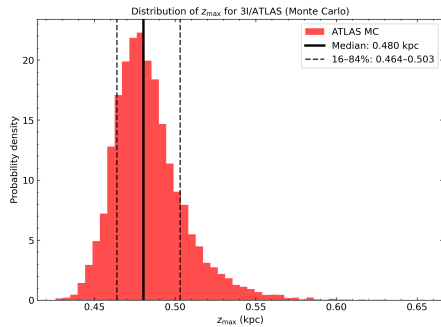


Fig. 6. Distribution of maximum vertical excursions z_{\max} for 3I/ATLAS from our Monte Carlo analysis. The vertical lines indicate the median and the 16th and 84th percentiles.

$z_{\max} = 0.481$ kpc. The 16th–84th percentile interval was 0.464–0.504 kpc, while the full Monte Carlo sample spanned 0.422–0.630 kpc. This high z_{\max} value, approaching half a kiloparsec, exceeds the scale heights of young thin-disk stars and solar-age populations. It is comparable to thick-disk vertical excursions and is therefore consistent with an older disk population under our adopted kinematic model.

3. Probability distribution of age

Next, we evaluate the probability distribution $p(t)$ (with unit normalization $\int p(t) dt = 1$) for the age t of the interstellar objects. This inference is conditioned on the hypothesis that the ISOs were produced by stellar populations in the Galactic disk and therefore sample the same underlying age distribution as those stars. We base our analysis on the extent of their vertical excursions, quantified by the maximum vertical value z_{\max} reached by their orbits, given that the disk scale height increases with stellar age. Possible nonstellar production channels (e.g., ejection from

giant molecular cloud environments or clustered star-forming regions) are acknowledged but not modeled here.

3.1. Bayesian statistical framework

We implemented a Bayesian statistical framework that combines the Monte Carlo orbital results with theoretical models of stellar kinematics. The likelihood was computed numerically by drawing vertical velocities, mapping them to turning points in the adopted vertical potential, and evaluating the empirical distribution of z_{\max} . For the prior, we used a digitized and tabulated approximation to the Milky Way star formation history inferred by Fantin et al. (2019), normalized over the age support (0–13.5 Gyr). We also report sensitivity to alternative priors in Appendix A.

3.1.1. Theoretical foundation

The Bayesian approach relies on the correlation between stellar age and vertical velocity dispersion in the Galactic disk. Young stellar populations exhibit smaller dispersions, while older populations show larger dispersions after long-term dynamical heating.

Our posterior probability for stellar age τ given observed maximum vertical height z_{\max} follows Bayes' theorem:

$$P(\tau|z_{\max}) \propto P(z_{\max}|\tau) \times \text{SFR}(\tau), \quad (1)$$

where $P(z_{\max}|\tau)$ is the likelihood function and $\text{SFR}(\tau)$ represents the star formation rate prior encoding when stars formed in Galactic history.

3.1.2. Likelihood

We compute $P(z_{\max}|\tau)$ from the vertical turning point condition in the adopted potential,

$$\frac{1}{2}v_z^2 + \Phi(z) = \Phi(z_{\max}), \quad (2)$$

so that $\Delta\Phi(z_{\max}) \equiv \Phi(z_{\max}) - \Phi(0) = \frac{1}{2}v_z^2$. Let $z_{\text{turn}}(v) \geq 0$ denote the nonnegative solution of $\Delta\Phi(z) = \frac{1}{2}v^2$. The induced likelihood is

$$P(z_{\max}|\tau) = \int_{-\infty}^{\infty} \mathcal{N}(v_z; 0, \sigma_W^2(\tau)) \delta[z_{\max} - z_{\text{turn}}(|v_z|)] dv_z, \quad (3)$$

which we evaluate using Monte Carlo draws of v_z , solving for z_{\max} in the adopted potential, and a kernel density estimate (KDE) of the resulting z_{\max} samples. We enforce the physical boundary $z_{\max} \geq 0$ by reflecting the KDE samples about zero, which removes bias near $z_{\max} = 0$.

3.1.3. Numerical implementation and convergence

The likelihood was evaluated on an age grid spanning 0–13.5 Gyr at 1 Myr resolution and used a cubic interpolant for the prior. At each age we drew $N_{v_z} = 600$ velocities from $\mathcal{N}(0, \sigma_W(\tau))$ with a fixed random seed and computed turning points in the adopted vertical potential. We estimated $P(z_{\max}|\tau)$ via KDE on the resulting z_{\max} samples. We verified stability by comparing 1 Myr versus 10 Myr grids and by extending the upper bound to 16 Gyr; posterior summaries are unchanged at the quoted precision.

3.1.4. Age-dependent velocity dispersion

We adopted a velocity dispersion model $\sigma_W(\tau)$ that captures thin and thick disk trends with a smooth transition. The thin disk

component follows a power law reflecting gradual dynamical heating:

$$\sigma_{\text{thin}}(\tau) = \sigma_1 \left(\frac{\tau}{1 \text{ Gyr}} \right)^\beta, \quad (4)$$

with $\sigma_1 = 8.0 \text{ km s}^{-1}$ and $\beta = 0.5$. The thick disk component uses a constant plateau $\sigma_{\text{thick}} = 40.0 \text{ km s}^{-1}$. To avoid an unphysical discontinuity, we blended these components smoothly via a tanh function:

$$f(\tau) = \frac{1}{2} \left[1 + \tanh \left(\frac{\tau - \tau_{\text{thick}}}{\Delta\tau} \right) \right], \quad (5)$$

$$\sigma_w(\tau) = \sqrt{(1-f)\sigma_{\text{thin}}^2(\tau) + f\sigma_{\text{thick}}^2}, \quad (6)$$

where $\tau_{\text{thick}} = 7.0 \text{ Gyr}$ marks the thin-thick transition and $\Delta\tau = 0.5 \text{ Gyr}$ controls the transition width. This smooth formulation avoids numerical artifacts while preserving the kinematic dichotomy; in the limit $\Delta\tau \rightarrow 0$, it recovers a sharp piecewise model.

The power-law component reflects gradual dynamical heating from gravitational scattering by giant molecular clouds and other perturbers (e.g., Kokubo & Ida 1992; Aumer & Binney 2009). With these parameters, $\sigma_w(10 \text{ Gyr}) \approx 40 \text{ km s}^{-1}$, consistent with thick-disk kinematics. The transition at 7 Gyr reflects the observed kinematic dichotomy in Galactic stellar populations, where stars older than this age exhibit systematically higher velocity dispersions, motivated by LAMOST-Gaia observations (Yu & Liu 2018). We explored 35–45 km s^{-1} plateaus and steeper exponents in sensitivity tests; in all cases, the resulting posterior median ages change by less than the reported credible intervals.

3.1.5. Star-formation-rate prior

We took a digitized and tabulated approximation to the Fantin et al. (2019) star formation history and defined the prior by normalization:

$$\text{SFR}_{\text{Fantin}}(\tau) \equiv \mathcal{I}_{\text{cub}}[\{\tau_i, \text{SFR}_i\}](\tau), \quad 0 \leq \tau \leq 13.5 \text{ Gyr}, \quad (7)$$

$$p(\tau) = \frac{\max(0, \text{SFR}_{\text{Fantin}}(\tau))}{\int_0^{13.5 \text{ Gyr}} \max(0, \text{SFR}_{\text{Fantin}}(t)) dt}. \quad (8)$$

Here \mathcal{I}_{cub} denotes a cubic interpolant of the digitized Fantin curve, and we set $\text{SFR}_{\text{Fantin}}(\tau) = 0$ outside the support. We truncated negative interpolated values to zero before renormalizing on the same support. We assessed prior sensitivity by comparing against an exponential form and a flat prior (see Appendix A).

3.2. Bayesian age inference results

The posterior age distributions for 1I/Oumuamua, 2I/Borisov, and 3I/ATLAS are shown in Figs. 7, 8, and 9, respectively, and are compared in Fig. 10. The Bayesian analysis yields age estimates that follow the expected trend with z_{max} :

- 1I/Oumuamua (young stellar system): median age of 3.2 Gyr with a 68% credible interval (CI) of 0.5–8.8 Gyr. The z_{max} value is consistent with a young origin, although the posterior retains a tail to older ages.
- 2I/Borisov (intermediate-age population): median age of 5.0 Gyr with a 68% credible interval of 1.8–9.7 Gyr. The moderate z_{max} indicates origin from thin disk stars with intermediate levels of dynamical heating.

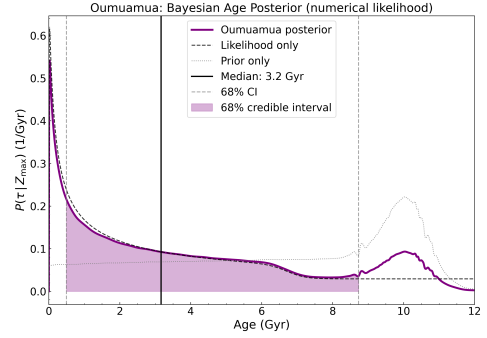


Fig. 7. Posterior age distribution for 1I/Oumuamua. The median age is 3.2 Gyr with a 68% CI [0.5, 8.8] Gyr.

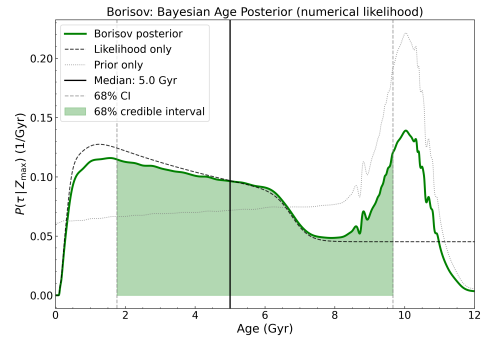


Fig. 8. Posterior age distribution for 2I/Borisov. The median age is 5.0 Gyr with a 68% CI [1.8, 9.7] Gyr.

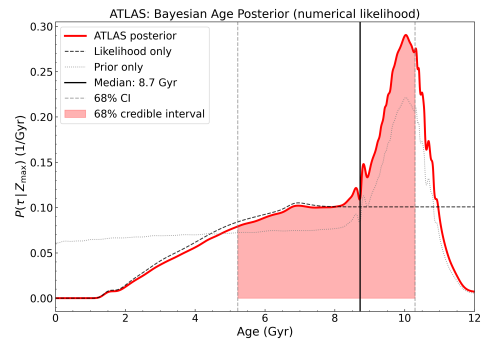


Fig. 9. Posterior age distribution for 3I/ATLAS. The median age is 8.7 Gyr with a 68% CI [5.2, 10.3] Gyr.

– 3I/ATLAS (older disk with thick-disk-like kinematics): median age of 8.7 Gyr with a 68% credible interval of 5.2–10.3 Gyr. The high z_{max} value requires high velocity dispersions characteristic of ancient thick disk populations. These classifications depend on the adopted age–velocity–dispersion relation and disk-heating model.

Our posteriors reflect two drivers: (i) the measured z_{max} , which sets the likelihood’s support across age and (ii) the star formation prior, which upweights epochs with higher stellar birth rates. For 1I and 2I, moderate z_{max} values favor thin-disk ages with broad tails; for 3I, the high z_{max} value shifts probability to older, thick-disk times. The widths of the credible intervals mainly trace measurement covariances in the inbound state and reasonable variations in $\sigma_w(\tau)$.

4. Discussion

Our Bayesian age inference results can be compared directly with previous investigations of interstellar object origins and ages, thereby providing context for our findings and clarifying

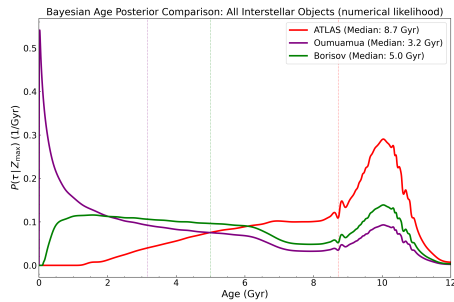


Fig. 10. Comparison of Bayesian age posteriors for all three interstellar objects. 1I/Oumuamua (purple), 2I/Borisov (green), and 3I/ATLAS (red) show distinct median ages.

methodological differences. For 1I/Oumuamua, Almeida-Fernandes & Rocha-Pinto (2018) inferred ages $\lesssim 2$ Gyr from kinematic arguments, broadly consistent with our median of 3.2 Gyr (68% CI: 0.5–8.8 Gyr). Hallatt & Wiegert (2020) argued for very young origins based on low velocity dispersions relative to the LSR; our credible interval does not include ages < 100 Myr. Hsieh et al. (2021) linked Oumuamua to nearby young associations (~ 30 Myr) via backtracking; differences relative to our results stem from methodology (association matching versus probabilistic kinematics). See also Gaidos, Williams & Kraus (2017) for an early young-association hypothesis. For 2I/Borisov, initial characterization showed typical cometary properties (Guzik et al. 2020). For 3I/ATLAS, Taylor & Seligman (2025) reported a kinematic age range of ~ 3 –11 Gyr under an equivalence assumption between ISO and stellar age–velocity relations; our median of 8.7 Gyr (68% CI: 5.2–10.3 Gyr) aligns with the older end of their interval. Recently, Hopkins et al. (2025) presented a related analysis of ISO kinematics and likewise found that 3I/ATLAS is consistent with an old disk population. Our results differ from Almeida-Fernandes & Rocha-Pinto (2018) primarily because they used the full 3D Galactocentric velocity, whereas we conditioned on the maximum vertical excursion z_{\max} .

Trajectory-based searches for stellar origins emphasize the difficulty of precise backtracking over long timescales owing to dynamical heating and measurement uncertainties (e.g., Bailer-Jones et al. 2018). Our approach complements these efforts by focusing on demographic age inference rather than on identifying specific progenitors. For priors on formation history, our baseline is a smooth interpolation to Fantin et al. (2019), with sensitivity to alternative priors shown in Appendix A.

5. Conclusions

We developed a framework for constraining the origins of interstellar objects through Galactic orbital analysis and Bayesian age inference. Our approach complements prior kinematic age inferences by focusing on z_{\max} -conditioned posteriors rather than full 3D velocities.

We performed ensemble calculations using 10 000 orbital realizations per object to account for measurement uncertainties in both interstellar object velocities and solar motion parameters. This approach yielded statistical distributions of maximum vertical excursions: $z_{\max} = 0.016 \pm 0.002$ kpc for 1I/Oumuamua, 0.121 ± 0.010 kpc for 2I/Borisov, and $0.481^{+0.023}_{-0.017}$ kpc for 3I/ATLAS.

We implemented a statistical framework that combines the orbital z_{\max} measurements with models of stellar kinematics. The methodology uses a numerical likelihood (with no closed form) and an age-dependent velocity dispersion that captures

observed thin–thick disk trends. Our analysis yields quantitative age estimates: 1I/Oumuamua is consistent with a young stellar system (3.2 Gyr, 68% CI: 0.5–8.8 Gyr), 2I/Borisov with an intermediate-age population (5.0 Gyr, 68% CI: 1.8–9.7 Gyr), and 3I/ATLAS with an older disk population (8.7 Gyr, 68% CI: 5.2–10.3 Gyr).

The results demonstrate the expected age trend in which smaller vertical excursions correspond to younger stellar origins. 1I/Oumuamua’s confined orbit is consistent with ejection from a relatively young stellar system in the thin Galactic disk. 2I/Borisov’s moderate excursions suggest an origin in a solar-age thin-disk population. 3I/ATLAS’s large vertical range is consistent with velocity dispersions characteristic of older disk populations. We refrain from attributing specific formation mechanisms for thick-disk stars, given ongoing debates. Our Bayesian framework links the orbital z_{\max} measurements to simple disk-heating models, providing a practical way to report age estimates with credible intervals. Over many orbital times, the trajectories are expected to migrate radially as a result of transient features such as spiral arms or the Galactic bar (Sellwood & Binney 2002). These constraints apply under the assumption that ISOs and disk stars have experienced comparable vertical heating in the Galactic potential; deviations from this assumption would shift the inferred ages. Excess ejection speeds relative to parent stars can shift the inferred ages in either direction; we did not explicitly model ejection-speed distributions here. We also refrain from inferring specific formation pathways from the current sample; the distinct median ages are consistent with multiple possible origins, but more objects will be required to draw firm demographic conclusions.

Data availability

Supplementary material supporting this article is available at Zenodo: <https://sandbox.zenodo.org/records/473317>

Acknowledgements. We thank Matthew Hopkins for his careful cross-checking of our paper. This work was supported in part by Harvard University, the Black Hole Initiative and the Galileo Project.

References

- Almeida-Fernandes, F., & Rocha-Pinto H. J. 2018, *MNRAS*, **480**, 4903
- Aumer, M., Binney, J. J. 2009, *MNRAS*, **397**, 1286
- Bailer-Jones, C. A. L., Farnocchia, D., Meech, K. J., Brassier, R., Micheli, M., Chakrabarti, S., Buie, M. W., et al. 2018, *AJ*, **156**, 205
- Bailer-Jones, C. A. L., Farnocchia, D., Ye, Q., Meech, K. J., Micheli, M. 2020, *A&A*, **634**, A14
- Sellwood, J. A., Binney, J. J. 2002, *MNRAS*, **336**, 785
- Fantin, N. J., Côté, P., McConnachie, A. W., et al. 2019, *ApJ*, **887**, 148
- Hallatt, T., Wiegert, P. 2020, *AJ*, **159**, 147
- Hsieh, C.-H., Laughlin, G., Arce, H. G. 2021, *ApJ*, **917**, 20
- Jewitt, D. 2024, *Handbook of Exoplanets*, Interstellar Objects in the Solar System (Berlin: Springer)
- Jewitt, D., & Seligman, D. Z. 2023, *Ann. Rev. Astron. Astrophys.*, **61**, 197
- Kokubo, E., Ida, S. 1992, *PASJ*, **44**, 601
- Loeb, A., MacLeod, M. 2024, *A&A*, **686**, A123
- Mamajek, E. 2017, *Res. Notes Am. Astron. Soc.*, **1**, 21
- Meech, K. J., Weryk, R., Micheli, M., et al. 2017, *Nature*, **552**, 378
- McMillan, P. J. 2017, *MNRAS*, **465**, 76
- Pöder, S., Benito, M., Pata, J., et al. 2023, *A&A*, **676**, A134
- Robin, A. C., Bienaymé, O., Salomon, J. B., et al. 2022, *A&A*, **667**, A98
- Siraj, A., Loeb, A. 2022a, *AsBio*, **22**, 1459
- Siraj, A., Loeb, A. 2022b, *ApJ*, **939**, 53
- Williams, G. V. 2017, *Minor Planet Electronic Circulars*, 2017-V17
- Yu, J., Liu, C. 2018, *MNRAS*, **475**, 1093
- Zhang, Y., Lin, D. N. C. 2020, *NatAs*, **4**, 852
- Hopkins, M. J., Dorsey, R. C., Forbes, J. C., et al. 2025, *ApJ*, **990**, L30
- Seligman, D. Z., Micheli, M., Farnocchia, D., et al. 2025, *ApJ*, **989**, L36
- Taylor, A. G., & Seligman, D. Z. 2025, *ApJ*, **990**, L14
- Gaidos, E., Williams, J., Kraus, A. 2017, *RNAAS*, **1**, 13
- Guzik, P., Drahus, M., Rusek, K., Waniak, W., et al. 2020, *NatAs*, **4**, 53

Appendix A: Diagnostics and sensitivity tests

This appendix provides supporting diagnostics for the Bayesian age inference described in Sect. 3, specifically the sensitivity of the posteriors to alternative star formation priors. The figures below (Figs. A.1–A.3) summarize these tests for each object.

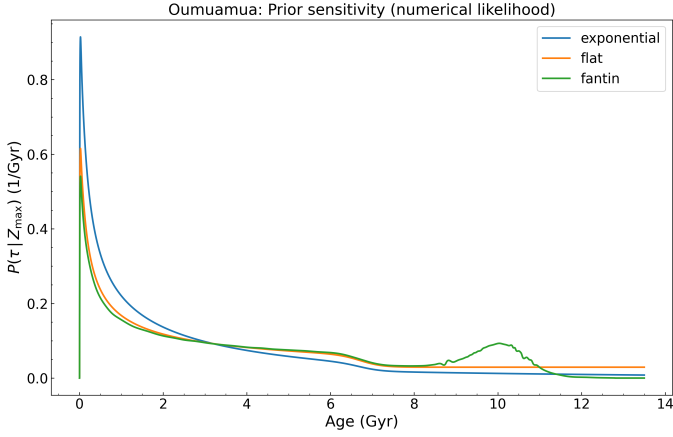


Fig. A.1. Prior sensitivity for 1I/Oumuamua. The posterior is recomputed using the Fantin prior, a flat prior, and an exponential prior.

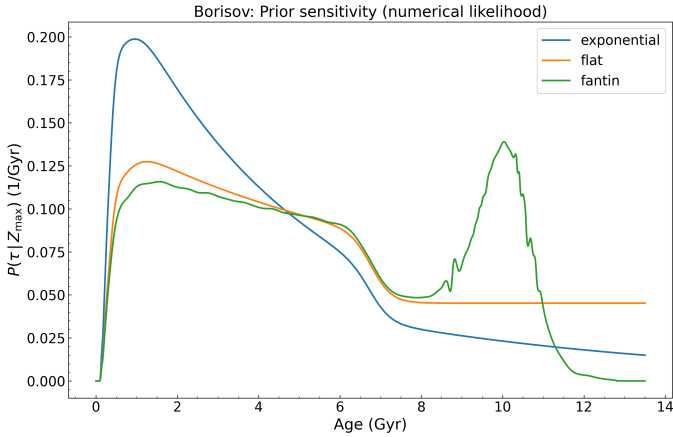


Fig. A.2. Prior sensitivity for 2I/Borisov. The posterior is recomputed using the Fantin prior, a flat prior, and an exponential prior.

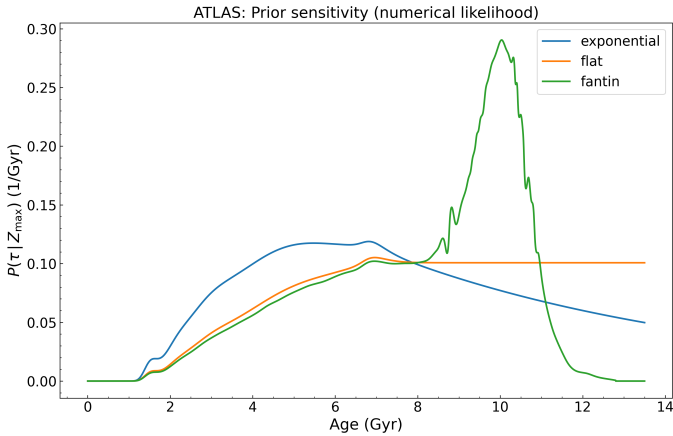


Fig. A.3. Prior sensitivity for 3I/ATLAS. The posterior is recomputed using the Fantin prior, a flat prior, and an exponential prior.